



CHORUS

This is the accepted manuscript made available via CHORUS. The article has been published as:

In situ study on the evolution of atomic and electronic structure of math

LaTiO_3 system

Hawoong Hong, Jessica L. McChesney, Friederike Wrobel, Xi Yan, Yan Li, Anand Bhattacharya, and Dillon D. Fong

Phys. Rev. Materials **6**, L011401 — Published 14 January 2022

DOI: [10.1103/PhysRevMaterials.6.L011401](https://doi.org/10.1103/PhysRevMaterials.6.L011401)

In situ Study on the Evolution of Atomic and Electronic Structure of LaTiO₃/SrTiO₃ System

Hawoong Hong^{1*}, Jessica L. McChesney^{1**}, Friederike Wrobel², Xi Yan², Yan Li^{2,3,4}, Anand Bhattacharya², Dillon D. Fong²

¹X-ray Science Division, Advanced Photon Source, Argonne National Laboratory, 9700 S. Cass Ave, Lemont, IL, 60439, United States

²Materials Science Division, Argonne National Laboratory, 9700 S. Cass Ave, Lemont, IL, 60439, United States

³Institute of High Energy Physics, Chinese Academy of Sciences, Beijing 100049, China

⁴University of Chinese Academy of Sciences, Beijing 100049, China

*e-mail: hhong@anl.gov

**e-mail: jmcchesn@anl.gov

Abstract

As with other transition-metal oxide interfaces, LaTiO₃/SrTiO₃ interfaces exhibit interesting electronic properties, such as a two-dimensional electron gas. While the available Mott states and multiple pathways to metallicity in LaTiO₃ can lead to a variety of applications in oxide electronics, the origin of the different properties remain uncertain. Utilizing real-time, in-situ X-ray diffraction at the synchrotron, robust but thin LaTiO₃/SrTiO₃ heterostructures were fabricated using oxide molecular beam epitaxy. A thickness of six unit-cells was determined to be critical, at which point the LaTiO₃ / SrTiO₃ heterostructures begin to sustain sharp, well-defined interfaces. The layers of LaTiO₃ and SrTiO₃ were sufficiently thin to benefit from the finite escape length of electrons at resonant soft X-ray photoemission, and the heterostructures were transferred *in vacuo* after growth to another chamber for synchrotron-based X-ray photoemission spectroscopy studies. With the X-ray energy tuned to the Ti-2*p* resonance, the LaTiO₃/SrTiO₃ interfaces could be probed with enough penetration depth and selectivity. It is shown that all of the heterointerfaces exhibit the 2-dimensional electron gas.

Interfaces between two different perovskite oxides continue to be investigated extensively due the novel electronic properties that can emerge such as the formation of a two-dimensional electron gas (2DEG) [1, 2, 3]. First reported for the (001) heterointerface between LaAlO₃ and SrTiO₃ (LAO/STO) [4], it was later revealed that in addition to oxide heterointerfaces a 2DEG is formed at the vacuum interface for cleaved SrTiO₃ [5]. These findings and others suggest that oxygen deficiency helps to induce 2DEG formation. However, there have also been efforts to attribute the 2DEG to the presence of quantum well states at the interface, in analogy with group IV and III/V systems, with states forming on the STO side of the interface due to the band bending [6]. Naturally, this has led to additional studies, including those on oxide superlattices and oxide-sandwiches, the latter consisting of a single unit cell (uc) of LaXO₃ or a single layer of a rare earth oxide sandwiched between STO layers. Exhibiting the standard quantum well geometry, these have proven to be clean and relatively simple systems for studying the origin of the 2DEG [7, 8, 9, 10] and investigating the effects of confinement [11, 12]. However, direct investigations of

the interfacial electronic structure have been limited to systems with relatively small overlayer thicknesses, i.e., up to a few monolayers. This is due to the relatively short penetration/escape depth of typical electronic probes, such as those used in angle-resolved photoelectron spectroscopy (ARPES).

Similar to LAO/STO, the interface between LaTiO_3 and SrTiO_3 (LTO/STO) has been described as a quantum well system [13, 14, 15, 16] although the usual spectroscopic signatures of quantum well states have hardly been found. This may be due in part to the complex properties of the transition metal oxides. While stoichiometric LTO is non-magnetic insulator at room temperature, it becomes an antiferromagnetic Mott insulator below 146 K [17, 18, 19, 20, 21]. Below this transition, two of the three $\text{Ti-}3d$ lower Hubbard bands (LHB) no longer lie just below the Fermi level but shift into the gap, reducing the charge transfer gap (gap between Ti and O derived states), and LTO becomes antiferromagnetic. Early work on LTO/STO heterostructures was focused on the properties of ultrathin LTO layers [1], including 2 unit cell (uc) LTO films on STO [22] and 1 uc LTO sandwiched between STO layers [23]. In this report, we discover that an LTO thickness of at least 6 uc is necessary for the synthesis of sharp, well-defined interfaces. We describe the atomic and electronic structures of a series of LTO/STO samples designed to probe the physics of the LTO/STO interface.

The LTO/STO heterostructures were grown on TiO_2 -terminated Nb-doped (0.5 wt.%) STO (001) using a molecular beam epitaxy (MBE) growth chamber mounted on and coupled to an X-ray diffractometer at Sector 33-ID of the Advanced Photon Source (APS) [24, 25]. Efficient determination of the proper growth conditions requires *in situ* monitoring of the film structure, as LTO growth at oxygen background pressures that are too high can lead to formation of the monoclinic structure ($\text{La}_2\text{Ti}_2\text{O}_7$) instead of LaTiO_3 [26] due to oxygen intercalation [27]. For films grown by pulsed laser deposition (PLD), researchers have found that the oxygen background must be below 1×10^{-4} torr for growth within the 650 - 900° C temperature range; growth above this pressure leads to $\text{La}_2\text{Ti}_2\text{O}_7$ [26]. In addition, although bulk LTO is an insulator, LTO films can be metallic for several different reasons. For example, when a film is tetragonally distorted due to the strain from the substrate, LTO films can become metallic [28, 29, 30]. Signatures of strain-induced metallicity are most apparent in films above ~ 4 uc in thickness [13]. Metallicity can also originate from a slight excess of oxygen [31]. As a result, the properties of LTO are highly sensitive to both stoichiometry and strain. We find that MBE offers improved control in terms of cation/anion stoichiometry and defect management, particularly when performed in coordination with *in situ* techniques.

The oxide MBE system is equipped with a reflection high energy electron diffraction (RHEED) system, several effusion cells, and a crystal thickness monitor. The LTO films were grown by co-deposition of lanthanum and titanium at 700°C in a background of oxygen. Oxygen partial pressures ranging from 1.5 to 2.5×10^{-8} Torr were maintained throughout deposition after ultra-high-vacuum (UHV) outgassing of the substrates at 300°C. The optimal deposition window was experimentally determined, with the relatively low oxygen pressure preventing the incorporation of excess oxygen into the film, and the moderately low growth temperature suppresses interdiffusion of oxygen from the substrate. STO deposition was performed by the shuttered growth technique, alternating between the strontium and titanium sources. Prior to growth, the STO substrates were processed to exhibit TiO_2 surface termination [32, 33]. We measured the specular rod immediately after growth and also after the sample was cooled to room temperature. All of the X-ray diffraction measurements were performed *in situ*. The MBE chamber is equipped with large Be windows to facilitate access to large volumes of reciprocal space and enable the immediate characterization of film structures as they form. The following three heterostructures were grown and studied: a single interface LTO/STO-substrate (sub), a double interface STO/ LTO/STO-sub, and a triple interface LTO/ STO/ LTO/STO-sub, where all of LTO and STO layers are 6 uc thick. They

are depicted in Figure. 1. Details on MBE growth and *in situ* X-ray diffraction measurements for the single interface sample and the double interface sample are provided in the reference 34.

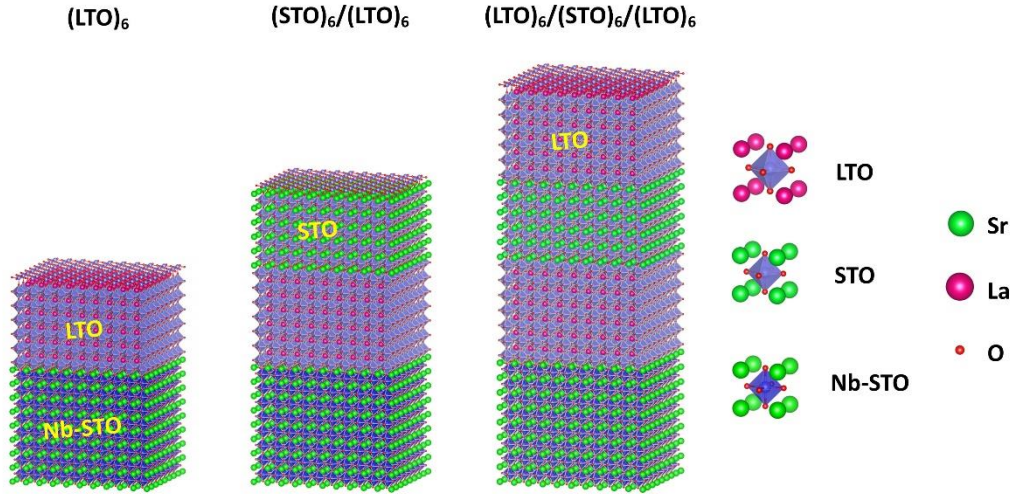


FIG. 1. Schematics of single, double, and triple $\text{LaTiO}_3/\text{SrTiO}_3$ heterostructures grown by oxide MBE on Nb:STO (001) substrates and alternating deposition of six unit cells of LaTiO_3 or SrTiO_3 .

During the growth of the triple interface sample, scans along the specular rod (00L scans) were repeated over the $L = 0.5$ to 1.5 range. These measurements were initiated at the completion of each unit cell. For each LTO unit cell, deposition took 389 seconds. The initial scan took 194 seconds. However, the scans were accelerated until the scan time became 110 sec by the start of the 5th LTO unit cell. Figure 2(b) and (c) show results from measurements taken during growth of first 6 uc of LTO and the subsequent 6 unit cells of STO, respectively. The deposition times during the STO cycle were 269 sec for Sr and 372 sec for Ti. The step-by-step increase in the number of interference fringes shows that the quality of the sample remains high during growth and that the quality of the sample was preserved. Figure 2(a) shows the 00L scan from the finished sample. The excellent contrast of the interference fringes between Bragg reflections up to high values of L indicates the growth of a sample with extremely smooth interfaces.

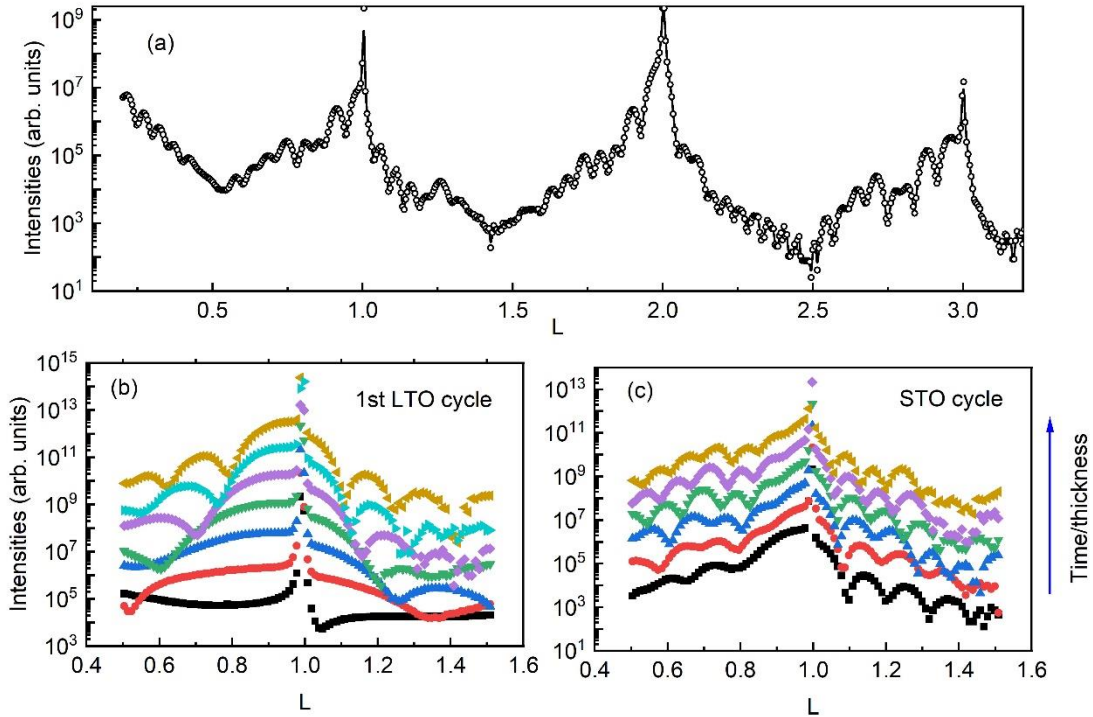


FIG. 2. (00L) scans during LTO/STO/LTO/Nb-STO(001) sample. (a) A wide-range scan from the completed sample. (b) Short-range pseudo-real time scans during first 6 uc LTO deposition. The bottom black squares are for the scan before the start of the deposition. Each scan was initiated at the end of one unit-cell formation. (c) Scans during STO cycle on first LTO layer.

After deposition, the as-grown samples were transferred to a UHV suitcase, which was kept under $< 10^{-9}$ Torr and connected to the oxide-MBE chamber through a load-lock. They were then moved to a soft x-ray ARPES chamber at 29-ID for spectroscopic characterization. Keeping the samples in UHV eliminates the need for a capping layer; X-ray photoemission spectroscopy (XPS) overview scans show only the constituent species, confirming that the samples remained pristine [34]. In addition, the use of a vacuum suitcase removes any need for *in situ* annealing, ensuring that the oxidation state for the samples remains unchanged between growth and spectroscopic measurements.

Angle-resolved photoemission spectroscopy (ARPES) data were taken both at the Ti-2*p* resonant energy ($h\nu = 460$ eV) in order to take advantage of the significant enhancement of signal observed when the photon energy matches an absorption edge. Figure 3 shows ARPES band dispersion at the zone center, taken on resonance. Normally in this energy range, the electron mean free path is ~ 1 nm [16] with the emitted electron intensities reduced by 90% after electrons travel through ~ 6 unit cells (2.4 nm). However, the probe depth at the Ti-2*p* energy is enhanced beyond 6 unit cells due to the resonance of the

Ti cations [35, 36], and our resonant spectra include information from buried interfaces. Using three samples with alternating LTO/STO stacks incrementally added, the interfaces are sequentially probed from the bottom. In this way, effective depth profiling of LTO/STO superstructure has been achieved. The ARPES intensities were integrated over the Brillouin zone to produce partial density-of-states (pDOS) plots. These are shown in Figure 3(d). The intensities from the single interface sample (6 uc LTO/STO-sub) are higher and scaled down by factor of 0.75 in the graph.

From the X-ray spectroscopy we observe the following trends on all three samples: as we tune the photon energy to the Ti-2*p* resonance we see the emergence of states within the band gap regardless of the exact surface termination. This includes the sharp peak crossing the Fermi level (corresponding to the 2DEG) and a broad feature centered at -1.1 eV, corresponding to the formation of a lower Hubbard band. The valence band, which consists primarily of oxygen-derived states, is consistent with the known surface termination of LTO or STO.

There are many reports [e.g., Ref. 37] that oxygen vacancies create a defect band at -1.3 eV. Aiura *et al.* observed that small amount of oxygen exposure (0.3 Langmuir) removed the -1.3 eV band and concluded that this band belongs to surface states [37]. It is also thought that these vacancies induce the 2DEG on STO surfaces. In addition, it has been observed that TiO₂-terminated STO actually has a double TiO₂ layer termination which is known to exhibit both oxygen deficiency and the 2DEG [38, 39]. However, unlike the defect band in STO, which due to the localized nature of the defects has no dispersion, this feature for the LTO terminated films is distinct both in a more narrow band width when compared to STO and broad dispersion [34]. The fact that the STO terminated films do not show a clear peak in the angle-integrated energy distribution curve, which represents the partial density of states (pDOS), corroborates the attribution of this feature to the LHB of LTO. Comparing the ratio of the intensity at the Fermi level with that of the valence band, we see that for the single interface LTO/STO-sub they are comparable while for the two and three interface films (STO/LTO/STO-sub and LTO/STO/LTO/STO-sub) it is significantly reduced. However, this does not suggest that the 2DEG exists only at the interface between the first LTO and the STO substrate as the decrease in intensity does not follow the exponential decay expected for a buried interface. Even for the Ti-2*p* resonance measurements, most of the photoemission intensities can be attributed to the interface nearest the surface. One cannot observe data from below the top two 6 unit cell overlayers (~1% transmission). This suggests that the 2DEG resides at each STO/LTO interface. Interestingly, we see that the ratio of the 2DEG to the Hubbard band in the LTO-terminated film is the same whether it is the LTO/STO-sub or the LTO/STO/LTO/STO-sub film. Due to the short electron inelastic mean free path, this depth dependence precludes attributing the LHB to oxygen deficiency at STO surface/interfaces.

The LTO/STO-sub film clearly has two different oxidation states, Ti⁴⁺ and Ti³⁺, as evidenced by the two peaks observed in the Ti-2*p* XPS and in the ratio of the L₂ and L₃ edges in the Ti-2*p* X-ray absorption spectrum (Supplemental Figure 5). There could be multiple pathways leading to Ti⁴⁺ peaks in LTO. As shown by Scheiderer *et al.* [19], it can come from extra oxidation at the topmost TiO₂ layer or oxygen diffusion from the substrate. However, the sample growth condition should suppress extra oxidation, and the X-ray diffraction data indicate very sharp interfaces between layers. Our case should be similar to one previously reported regarding charge redistribution at polar/non-polar interfaces as determined from STEM-EELS (scanning transmission electron microscopy-energy loss spectroscopy) [1]. In the La₂Ti₂O₇ phase, all of Ti ions are 4+. However, to form the La₂Ti₂O₇ phase in the film, far higher oxygen pressure is required than the oxygen pressure used in the present study [26, 27]. More importantly, the synchrotron X-ray diffraction data do not provide any evidence of La₂Ti₂O₇.

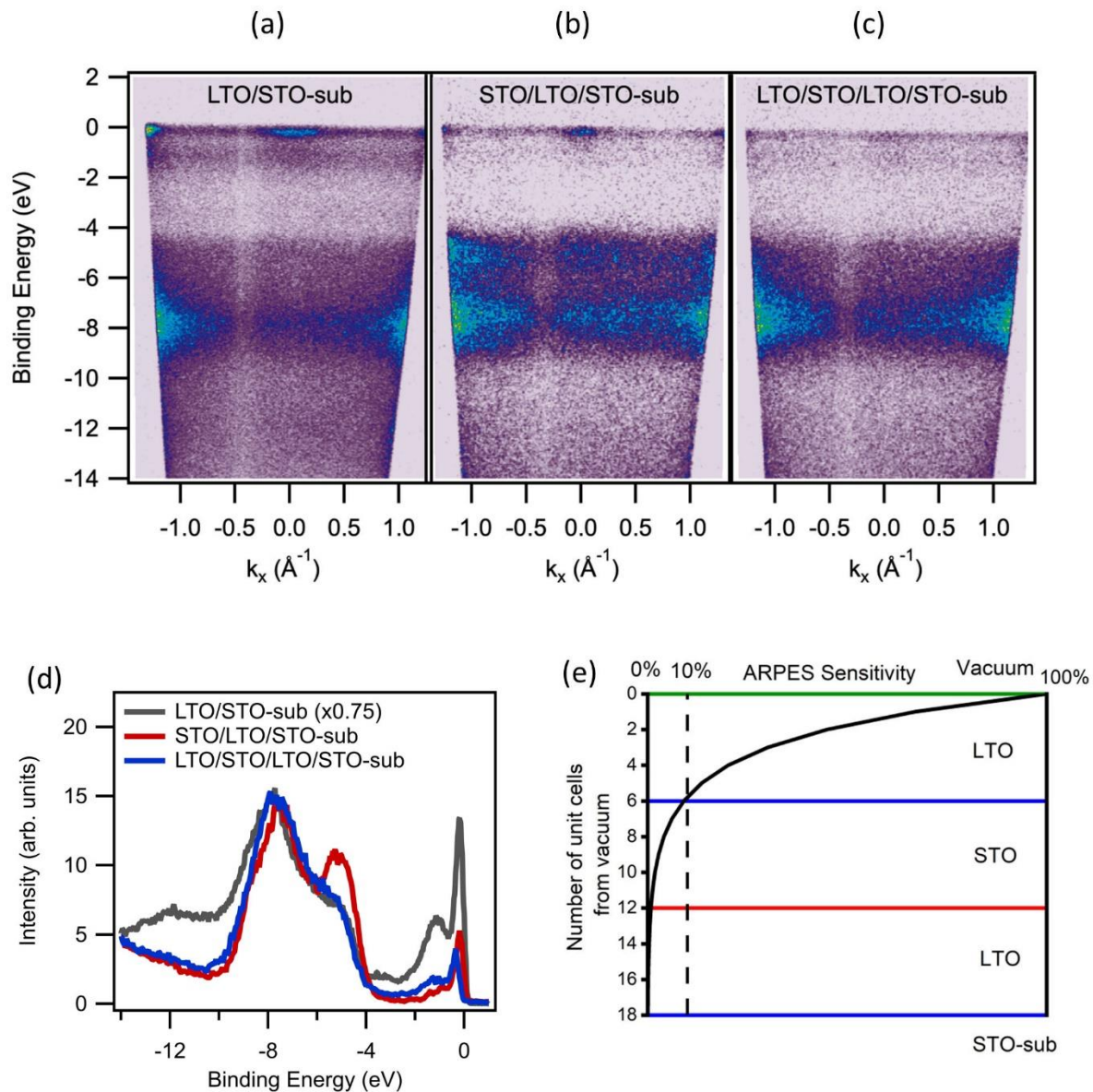


FIG. 3. Band dispersion at the zone center with incoming photon energy at Ti-2*p* resonance (460eV) for (a) a single LTO/STO interface, 6 uc LTO on STO-sub (001) (b) a double LTO/STO interface, 6 uc STO/ 6 uc LTO/ STO-sub (001) and (c) a triple LTO/STO interface, 6 uc LTO/6 uc STO/ 6 uc LTO/ STO-sub (001). The color scale was adjusted individually for maximum contrast. (d) pDOS from integration of ARPES over Brillouin zone. (e) ARPES sensitivities through the slabs from electron escape length.

Previous photoelectron spectroscopy measurements ($h\nu=21.2$ eV) by Takizawa *et al.* on 2 uc LTO show a similar feature at ~ -1 eV [22]. These samples were capped with 2 uc STO. Their spectrum exhibits band gaps from 3 to 4 eV, and the valence band maxima are similar to those shown here, in agreement with other theoretical and experimental works [22]). The sharp peaks near the Fermi level are from the Ti-3d states. While these states correspond to the 2DEG, it is uncertain whether the 2DEG originates from TiO₂-terminated STO or from the LTO/STO interfaces. For these heterostructures, only the double interface sample (6 uc STO/ 6 uc LTO/ STO-sub) has a TiO₂-terminated STO layer at the top, dominating the photoemission signal. The 2DEG near the Fermi level on this sample is the weakest among three, suggesting that the 2DEG originates at the LTO/STO interfaces. Chang *et al.* investigated the evolution of the band structure of 1 uc LTO and with subsequent STO overlayers, finding that the 2DEG persists as the LTO is buried [23]. Unlike in the present study, a thick, insulating STO buffer layer was first deposited on the initial Nb-doped STO substrate, and they found a very clean gap without a 2DEG. This agrees with the claim that the TiO₂ termination of STO by itself is not a sufficient condition for the formation of a 2DEG [40]. Another salient but puzzling feature is that the single interface sample (6 uc LTO/STO-sub) has non-zero pDOS in the gap around -3.5 eV.

As mentioned earlier, bulk LTO transitions to an antiferromagnetic Mott insulator below 146 K. ARPES measurements on the single interface sample were recorded at 175 K and 30 K to probe the opening of a Mott gap; probing the antiferromagnetic ordering is outside the scope of the experiments presented here. The results are shown in Figure 4. The ARPES map at 175 K appears to have a higher background and a diffuse intensity distribution than the one at 30 K since the phonon scattering modes are not frozen out at these higher temperatures. When the high temperature data are scaled up by factor of 1.5, the pDOS for the two temperatures show little difference in the line shape, and the curves overlay. For all temperatures, the density of states near the Fermi level are dominated by the 2DEG and the Mott gap is not detectable. However, in addition to the 2DEG being stable at both temperatures, we observe no shift in position or intensity for the lower Hubbard band at ~ -1 eV and no any change in the position of the valence states between -4 and -12 eV binding energy, suggesting that there is no metal-insulator transition. According to theory [17], the lower Hubbard bands should move down to the band gap by ~ 2 eV and leave the upper Hubbard band at the conduction band when going through the transition. This should result in changes to the band gap and the density of states near the Fermi level. The DFT calculation in Ref. 17 shows changes to lower-occupied Hubbard band on the order of 1 eV at the $\bar{\Gamma}$ point. However, the DFT calculation does not agree with experiment in its estimation of the Mott gap. The experimental Mott gap is about 0.1 eV [18, 19], and the DFT results predict far larger Mott gaps [17]. The transition to an antiferromagnetic phase may be obscured by the 2DEG density of states or be too subtle for this experiment, where the experimental resolution was 250 meV. However, it is also likely that the 6 unit cell LTO is not thick enough to develop electronic properties similar to the bulk phase. The EELS results from Ohtomo *et al.* study clearly show the emergence of bulk-like charge states near the center of LTO only after the film is sufficiently thick [1].

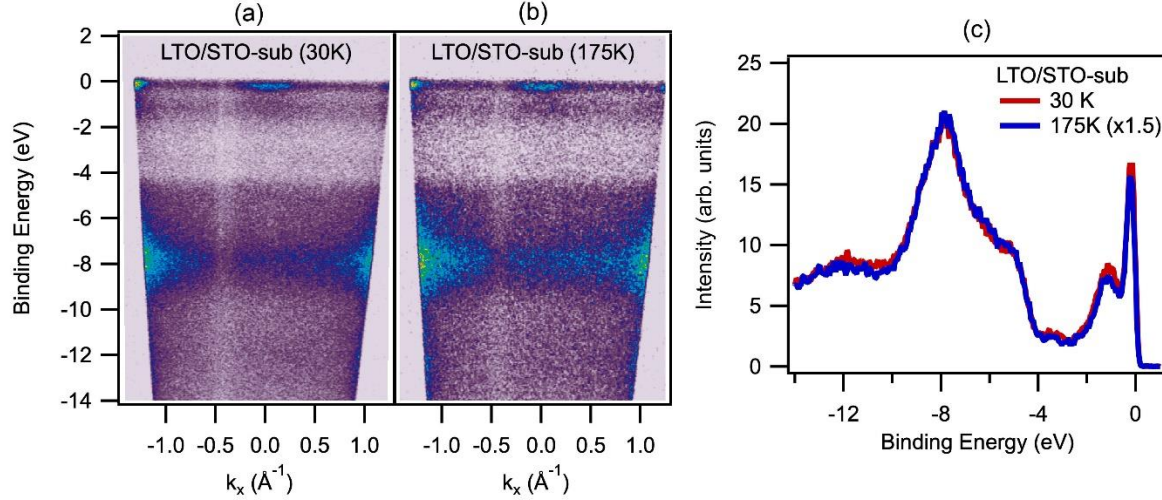


FIG. 4. ARPES map of the single interface sample (6 uc LTO/STO-s) and PDOS plot. (a) At 175 K above phase transition. (b) At 30K. Color scales are separately made. (c) PDOS from two temperatures.

In summary, in order to probe the relationship between Mott physics and the formation of a 2DEG, three heterostructures with a multiple number of LTO/STO interfaces were synthesized sequentially to probe one interface at a time. The choice of individual film thicknesses was made to guarantee high quality heterostructures and allow ARPES studies of the interfaces. This allows interface-by-interface selectivity in the spectroscopy. Exploiting the Ti- $2p$ resonance and alternating layer stacking sequence, we are able spectroscopically probe the LTO/STO-sub, STO/LTO and LTO/STO interfaces. Utilizing *in situ* X-ray diffraction in real time, the film structure was monitored during oxide MBE growth of each layer. This allowed the determination of the thickness necessary for achieving well-defined LTO heterostructures and help to guarantee the interfacial integrity of the fabricated samples. The samples were kept clean and moved to another location for ARPES in a UHV suitcase, avoiding the need of a capping layer or *in situ* cleaning. Soft X-rays at Ti- $2p$ resonance were used to enhance penetration to deeper interfaces (more than for ultra-violet wavelengths). The ARPES measurements here in combination with previous work suggest that the observed 2D electron gases are from LTO/STO interfaces and not from the TiO₂-terminated STO surface. Temperature-dependent ARPES measurements did not show any change in the lower Hubbard band through the bulk phase transition, which runs counter to the DFT calculation. Our study demonstrates the benefit of multi-modal investigations for understanding the structural and electronic properties of oxide interfaces.

Acknowledgement

The authors are grateful to Prof. K. Zou of University of British Columbia for advice on the growth of LTO films. D.D.F. was supported by the U.S. Department of Energy, Office of Science, Basic Energy Sciences, Materials Sciences and Engineering Division. Work performed at the Advanced Photon Source at Argonne National Laboratory was supported by the U.S. Department of Energy (DOE), Basic Energy Sciences, under Contract No. DE-AC02-06CH11357. This material is also based upon work supported

by Laboratory Directed Research and Development (LDRD) funding from Argonne National Laboratory, provided by the Director.

References

1. A. Ohtomo, D. Muller, J. L. Grazul, H. Y. Hwang, *Nature* **419**, 378 (2002).
2. J. Biscaras, N. Bergeal, S. Hurand, C. Grossetête, A. Rastogi, R. C. Budhani, D. LeBoeuf, C. Proust, and J. Lesueur, *Phys. Rev. Lett.* **108**, 247004 (2012).
3. E. N. Jin, L. Kornblum, D. P. Kumah, K. Zou, C. C. Broadbridge, J. H. Ngai, C. H. Ahn, and F. J. Walker, *APL Materials* **2**, 116109 (2014).
4. A. Ohtomo, and H. Y. Hwang, *Nature* **427**, 423 (2004).
5. A. F. Santander-Syro, O. Copie, T. Kondo, F. Fortuna, S. Pailhès, R. Weht, X. G. Qiu, F. Bertran, A. Nicolaou, A. Taleb-Ibrahimi, P. Le Fèvre, G. Herranz, M. Bibes, N. Reyren, Y. Apertet, P. Lecoeur, A. Barthélémy, and M. J. Rozenberg, *Nature* **469**, 189 (2011).
6. J. Biscaras, S. Hurand, C. Feuillet-Palma, A. Rastogi, R. C. Budhani, N. Reyren, E. Lesne, J. Lesueur, and N. Bergeal, *Sci. Rep.* **4**, 6788 (2015).
7. H. W. Jang, D. A. Felker, C. W. Bark, Y. Wang, M. K. Niranjana, C. T. Nelson, Y. Zhang, D. Su, C. M. Folkman, S. H. Baek, S. Lee, K. Janicka, Y. Zhu, X. Q. Pan, D. D. Fong, E. Y. Tsymbal, M. S. Rzechowski, C. B. Eom, *Science* **331**, 886 (2011).
8. J. S. Kim, S. S. A. Seo, M. F. Chisholm, R. K. Kremer, H.-U. Habermeier, B. Keimer, and H. N. Lee, *Phys. Rev. B* **82**, 201407(R) (2010).
9. P. Larson, Z. S. Popović, and S. Satpathy, *Phys. Rev. B* **77**, 245122 (2008).
10. S. Okamoto, A. J. Millis, and N. A. Spaldin, *Phys. Rev. Lett.* **97**, 056802 (2006).
11. J. E. Ortmann, N. Nookala, Q. He, L. Gao, C. Lin, A. B. Posadas, A. Y. Borisevich, M. A. Belkin, and A. A. Demkov, *ACS Nano*, **12**, 7682 (2018).
12. M. Choi, C. Lin, M. Butcher, C. Rodriguez, Q. He, A. B. Posadas, A. Y. Borisevich, S. Zollner, and A.A. Demkov, *Appl. Phys. Lett.* **106**, 192902 (2015).
13. M. J. Veit, R. Arras, B.J. Ramshaw, R. Pentcheva, and Y. Suzuki, *Nat. Commun.* **9**, 1458 (2018).

14. H. Chen, A. Kolpak, and S. Ismail-Beigi, *Phys. Rev. B* **82**, 085430 (2010).
15. G. Berner, M. Sing, H. Fujiwara, A. Yasui, Y. Saitoh, A. Yamasaki, Y. Nishitani, A. Sekiyama, N. Pavlenko, T. Kopp, C. Richter, J. Mannhart, S. Suga, and R. Claessen, *Phys. Rev. Lett.* **110**, 247601 (2013).
16. C. Cancellieri, M. L. Reinle-Schmitt, M. Kobayashi, V. N. Strocov, T. Schmitt, P. R. Willmott, S. Gariglio, and J.-M. Triscone, *Phys. Rev. Lett.* **110**, 137601 (2013).
17. F. El-Mellouhi, E. N. Brothers, M. J. Lucero, I. W. Bulik, and G. E. Scuseria, *Phys. Rev. B* **87**, 035107 (2013)
18. T. Arima, Y. Tokura, and J. B. Torrance, *Phys. Rev. B* **48**, 17006 (1993).
19. P. Scheiderer, M. Schmitt, J. Gabel, M. Zapf, M. Stübinger, P. Schütz, L. Dudy, C. Schlueter, T.-L. Lee, M. Sing, and R. Claessen, *Adv. Mater.* **30**, 1706708 (2018).
20. F. El-Mellouhi, E. N. Brothers, M. J. Lucero, and G. E. Scuseria, *Phys. Rev. B* **84**, 115122 (2011).
21. B. Keimer, D. Casa, A. Ivanov, J. W. Lynn, M. v. Zimmermann, J. P. Hill, D. Gibbs, Y. Taguchi, and Y. Tokura, *Phys. Rev. Lett.* **85**, 3946 (2000).
22. M. Takizawa, H. Wadati, K. Tanaka, M. Hashimoto, T. Yoshida, A. Fujimori, A. Chikamatsu, H. Kumigashira, M. Oshima, K. Shibuya, T. Mihara, T. Ohnishi, M. Lippmaa, M. Kawasaki, H. Koinuma, S. Okamoto, and A. J. Millis, *Phys. Rev. Lett.* **97**, 057601 (2006).
23. Y. J. Chang, L. Moreschini, A. Bostwick, G. A. Gaines, Y. S. Kim, A. L. Walter, B. Freelon, A. Tebano, K. Horn, and E. Rotenberg, *Phys. Rev. Lett.* **111**, 126401 (2013).
24. T. K. Andersen, S. Cook, E. Benda, H. Hong, L. D. Marks, and D. D. Fong, *Rev. Sci. Instrum.* **89**, 033905 (2018).
25. J. H. Lee, I. C. Tung, S.-H. Chang, A. Bhattacharya, D. D. Fong, J. W. Freeland, and H. Hong, *Rev. Sci. Instrum.* **87**, 013901 (2016).
26. A. Ohtomo, D. A. Muller, J. L. Grazul, and H. Y. Hwang, *Appl. Phys. Lett.* **80**, 3922 (2002).
27. J. W. Seo, J. Fompeyrine, H. Siegwart, and J.-P. Locquet, *Phys. Rev. B* **63**, 205401 (2001).

28. F. J. Wong, S.-H. Baek, R. V. Chopdekar, V. V. Mehta, H.-W. Jang, C.-B. Eom, and Y. Suzuki, *Phys. Rev. B* **81**, 161101(R) (2010).
29. S. Okamoto, and A. J. Millis, *Nature* **248**, 630 (2004). Seo
30. S. S. A. Seo, W. S. Choi, H. N. Lee, L. Yu, K. W. Kim, C. Bernhard, and T. W. Noh, *Phys. Rev. Lett.* **99**, 266801 (2007).
31. Y. Okimoto, T. Katsufuji, Y. Okada, T. Arima, and Y. Tokura, *Phys. Rev. B* **51**, 9581 (1995).
32. M. Kawasaki, K. Takahashi, T. Maeda, R. Tsuchiya, M. Shinohara, O. Ishiyama, T. Yonezawa, M. Yoshimoto, H. Koinuma, *Surf. Sci.* **266**, 1540 (1994).
33. G. Koster, B. L. Kropman, G. J. H. M. Rijnders, D. H. A. Blank, and H. Rogalla, *Appl. Phys. Lett.*, **73**, 2920 (1998).
34. See Supplemental Material at [URL] for i. details of growth and X-ray diffraction, ii. XPS overview scans, and iii. ARPES maps.
35. C. Cancellieri, M. L. Reinle-Schmitt, M. Kobayashi, V. N. Strocov, P. R. Willmott, D. Fontaine, Ph. Ghosez, A. Filippetti, P. Delugas, and V. Fiorentini, *Phys. Rev. B* **89**, 121412(R) (2014).
36. G. Van der Laan, and B. T. Thole, *J. Phys. Condens. Matter* **7**, 9947 (1995).
37. Y. Aiura, I. Hase, H. Bando, T. Yasue, T. Saitoh, and D. S. Dessau, *Surf. Sci.* **515**, 61 (2002).
38. R. Shimizu, K. Iwaya, T. Ohsawa, S. Shiraki, T. Hasegawa, T. Hashizume, and T. Hitosugi, *Appl. Phys. Lett.* **100**, 263106 (2012).
39. S. Cook, K. Letchworth-Weaver, I.-C. Tung, T. K. Andersen, H. Hong, L. D. Marks, and D. D. Fong, *Sci. Adv.* **5**, eaav0764 (2019).
40. S. N. Rebec, T. Jia, H. M. Sohail, M. Hashimoto, D. Lu, Z.-X. Shen, and R. G. Moore, *PNAS*, **116** (34) 16687 (2019).